International Forum on Aeroelasticity and Structural Dynamics
IFASD 2017
25-28 June 2017 Como, Italy

INFLUENCE OF AERODYNAMIC NONLINEARITY ON FLUTTER OF CURVED PANELS AT TRANSONIC AND LOW SUPERSONIC MACH NUMBERS

Manav Bhatia[1] and Philip S. Beran[2]

[1]Department of Aerospace Engineering and Center for Advanced Vehicular Sytstems
Mississippi State University, Mississippi State 39759 USA
mb2908@msstate.edu

[2]Air Force Research Laboratory
Wright Patterson Air Force Base, Dayton OH 45433
philip.beran@us.af.mil

Keywords: Computational aeroelasticity, Transonic Flutter, Computational Fluid Dynamics

Abstract: This study focuses on assessing the influence of aerodynamic nonlinearity on the flutter characteristics of a curved semi-infinite panel at transonic and low supersonic Mach numbers. The fluid flow is modeled with compressible Euler equations and discretized using density-based streamline-upwind Petrov Galerkin finite element variational form. The structure is analyzed using finite element discretization of a linear Timoshenko beam model. The curved shape of the panel is defined by a half-sine bump with increasing amplitude. Steady-state flow is calculated for this shape and a linearization about this state is used to solve for the flutter mode using a small-disturbance stability eigenvalue formulation. The flutter characteristics are studied for increasing height of the panel curve at Mach 0.9, 1.1 and 1.5. At subsonic Mach numbers flow over the curved panel creates a supersonic bubble and at a sufficiently large height changes the instability mode from zero-frequency divergence to oscillatory flutter. At low supersonic Mach numbers the increasing curve height creates a subsonic region over the panel with a change in the composition of the resulting flutter mode. While the flutter speed is seen to monotonically increase at Mach 1.1, large reductions are observed at Mach 1.5.

1 Introduction

Flutter at transonic and low supersonic Mach numbers continues to pose a challenge for wing and airframe structural design [1]. Renewed interest in sustained supersonic and hypersonic flight has further amplified this challenge for thermally-stressed structures. Flight of a vehicle through the transonic regime after an extended heat soak at supersonic Mach numbers requires careful consideration of aeroelastic stability of structures under the influence of high temperatures. Bhatia and Beran [2,3] designed a thermally stressed semi-infinite panel subject to transonic flutter constraints and identified that structural nonlinearity can play an important role in design of such structures. Small imperfections in the panel can lead to quasi-static thermoelastic deformations, with influence on the steady-state flow and dynamic instability characteristics. This study calculated the

flutter modes assuming a uniform aerodynamic flow for the deformed panel, i.e. the structural quasi-static deformation included only the thermoelastic response while neglecting aerodynamic loads. While this cited study included only the influence of structural nonlinearity in transonic flutter, the present paper extends this investigation with the objective to understand the influence of aerodynamic nonlinearity on the flutter characteristics of curved panels.

Dynamic stability of curved panels has been studied by Dowell [4, 5], Cheng and Mei [6], Abbas, et al [7] and Cullers and McNamara [8]. All of these studies have focussed on supersonic Mach numbers with various forms of linear/non-linear piston theory. Structural nonlinearity has also been included to account for the influence of curvature and in-plane stresses. Dowell [4, 5] found that cross-stream curvature stabilizes the panel with strong dependence on in-plane edge restraint. All studies concluded that streamwise curvature can considerably alter the dynamic stabilities of a panel. Cullers and McNamara [8] found that high dynamic pressure loading can cause a thermally deformed panel to exhibit snap-through response.

The present study focuses on assessing the influence of aerodynamic nonlinearity on dynamic stability of a curved semi-infinite panel at transonic and low supersonic Mach numbers. The fluid flow is modeled with compressible Euler equations and discretized using density-based streamline-upwind Petrov Galerkin finite element variational form [9–11]. Some simplifying assumptions are made in order to maintain this focus. First, the structure is modeled with a linear Timoshenko beam theory. Second, a uni-directional coupling is assumed to calculate the steady-state flow, such that the aerodynamic flow is calculated about the curved panel shape, but it does not influence the quasi-steady panel deformation. These assumptions ensure that aerodynamics is the only source of nonlinearity in the stability analysis. A linearization about this steady-state serves as the basis for $V-g$ flutter solution approach [9, 11].

The paper is organized as follows. The function spaces used in the finite element discretization are defined in Sec. 2.1. The structural model is described in Sec. 2.2, and the fluid model is described in Sec. 2.3. An attempt has been made to maintain brevity of discussion in order to reserve space for the presentation of results, which are presented in Sec. 3. Finally, the conclusions are presented in Sec. 4.

2 Fundamental Equations

2.1 Finite Element Function Space

The plate structural model in this paper includes three variables, $\boldsymbol{x}_{\rm s} = \{u_z, \theta_x, \theta_y\}^T$, which are the displacement along $z-$axis and rotations about $x-$ and $y-$axes. Variable θ_x is excluded for the beam model. The C^0 continuous functional space for the structural deformation is a complete polynomial with compact support over each element, Ω_e, i.e.

$$\mathcal{V}_{\rm s}^h = \{\boldsymbol{x}_{\rm s} | \boldsymbol{x}_{\rm s} \in \left(\mathcal{C}^0(\Omega)\right)^m, \boldsymbol{x}_{\rm s}|_{\Omega_e} \in \left(\mathcal{P}_k(\Omega_e)\right)^m\}, \tag{1}$$

where, $m = 2$ for beams and $m = 3$ for plates, and k identifies the order of a complete polynomial $\mathcal{P}_k(\Omega_e)$ over the element domain Ω_e such that $\Omega = \bigcup_{e=1}^{N_{el}} \Omega_e$. The virtual

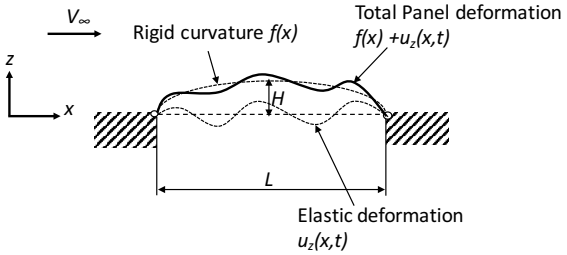

Figure 1: A semi-infinite panel under the influence of aerodynamic flow on one side.

displacements, $\delta\boldsymbol{x}_\mathrm{s}$, are additionally zero over the boundary with Dirichlet conditions (Γ_D), and the space is defined as

$$\mathcal{W}_\mathrm{s}^h = \{\boldsymbol{x}_\mathrm{s} | \boldsymbol{x}_\mathrm{s} \in \left(\mathcal{C}^0(\Omega)\right)^m, \boldsymbol{x}_\mathrm{s}|_{\Omega_e} \in (\mathcal{P}_k(\Omega_e))^m, \boldsymbol{x}_\mathrm{s}|_{\Gamma_D} = 0\}. \tag{2}$$

The fluid solution, $\boldsymbol{x}_\mathrm{f}$, for a $d-$dimensional flow problem has $d+2$ variables. Hence, the function space for the solution is defined as

$$\mathcal{V}_\mathrm{f}^h = \{\boldsymbol{x}_\mathrm{f} | \boldsymbol{x}_\mathrm{f} \in \left(\mathcal{C}^0(\Omega)\right)^{d+2}, \boldsymbol{x}_\mathrm{f}|_{\Omega_e} \in (\mathcal{P}_k(\Omega_e))^{d+2}\}. \tag{3}$$

The solution is approximated over each element domain using the shape functions and the vector of discrete coefficients. For example, $u_z(\xi) = \sum_i N_i(\xi) U_{zi}^e$, $i = 1, \ldots, n_\mathrm{shape}$, where, $N_i(\xi)$ is the i^th shape function at element coordinate ξ, n_shape is the number of shape functions corresponding to a variable on the element, and U_{zi}^e are the discrete coefficients corresponding to the shape functions over the element domain Ω_e. The same procedure is used to discretize all variables (structural and fluid). The vector of all discrete coefficients for the structural and fluid models are represented by X_s and X_f, respectively.

2.2 Structural Model

This paper considers the response of a semi-infinite panel exposed to aerodynamic flow on one side (Fig. 1). It is assumed that the lower side of the panel is exposed to the far-field pressure p_∞. The aerodynamic shape is defined by a combination of the rigid shape $f(x)$ and the elastic deformation $u_z(x,t)$. The former is pre-defined while the latter is identified from the stability eigensolution.

The panel is modeled using the Timoshenko beam theory that accounts for constant transverse shear strain through the thickness of the beam. The governing equations in the $x, z-$plane are characterized by the deformation, $u_z = u_z(x,t)$ and rotation of normals about the $y-$axis, $\theta_y = \theta_y(x,t)$:

$$\begin{aligned}
u_x &= z\theta_y, && (4)\\
\boldsymbol{\epsilon}_\mathrm{s}(\boldsymbol{x}_\mathrm{s}) &= \{\epsilon_{xx}, \gamma_{xy}\}^T = \boldsymbol{D}_s \boldsymbol{x}_s, && (5)\\
\boldsymbol{x}_s &= \{u_z, \theta_y\}^T, && (6)\\
\boldsymbol{D}_s &= \begin{bmatrix} 0 & z\partial/\partial x \\ \partial/\partial x & 1 \end{bmatrix}, && (7)\\
\boldsymbol{\sigma}_\mathrm{s}(\boldsymbol{x}_\mathrm{s}) &= \{\sigma_{xx}, \tau_{xz}\}^T = \boldsymbol{C}\boldsymbol{\epsilon}_\mathrm{s}(\boldsymbol{x}_\mathrm{s}), && (8)\\
\boldsymbol{C} &= \mathrm{diag}(E, G). && (9)
\end{aligned}$$

The governing equations and discretizations are defined on the reference undeformed configuration [11]. Note that this work assumes a unidirectional coupling for the steady-state flow such that the structure is not influenced by the steady-state flow about the shape defined by $f(x)$. Hence, the structural steady-state condition is defined by the undeformed state of the flat panel, implying that calculation of $\boldsymbol{x}_\mathrm{s}$ is not needed. A more general fluid-structure interaction problem would require the solution of the coupled steady-state equilibrium condition.

Assuming simple harmonic motion, $\boldsymbol{x}_\mathrm{s}(t) = \exp(i\omega_k t)\boldsymbol{y}_{sk}$, variational statement for the modal eigenproblem is stated as: find $(\omega_k, \boldsymbol{y}_{sk})$, with $\boldsymbol{y}_{sk} \in \mathcal{W}_\mathrm{s}^h$, such that for all $\delta\boldsymbol{x} \in \mathcal{W}_\mathrm{s}^h$

$$-\omega_k^2 \rho_\mathrm{s} \int_{-h/2}^{h/2} \int_\Omega \delta\boldsymbol{x}_\mathrm{s} \boldsymbol{y}_{sk} \; d\Omega \; dz + \int_{-h/2}^{h/2} \int_\Omega \boldsymbol{\epsilon}(\delta\boldsymbol{x}_\mathrm{s})^T \boldsymbol{\sigma}(\boldsymbol{y}_{sk}) \; d\Omega \; dz = 0, \tag{10}$$

which is expressed in matrix form as

$$\left(-\omega_k^2 \boldsymbol{M}_\mathrm{ss} + \boldsymbol{J}_\mathrm{ss}\right) Y_{sk} = 0. \tag{11}$$

The matrices are related to the variational statement as

$$\delta X_\mathrm{s}^T \boldsymbol{M}_\mathrm{ss} Y_{sk} = \rho_\mathrm{s} \int_{-h/2}^{h/2} \int_\Omega \delta\boldsymbol{x}_\mathrm{s}^T \boldsymbol{y}_{sk} \; d\Omega \; dz, \tag{12}$$

$$\delta X_\mathrm{s}^T \boldsymbol{J}_\mathrm{ss} Y_{sk} = \int_{-h/2}^{h/2} \int_\Omega \boldsymbol{\epsilon}_\mathrm{s}(\delta\boldsymbol{x}_\mathrm{s})^T \boldsymbol{\sigma}_\mathrm{s}(\boldsymbol{y}_{sk}) \; d\Omega \; dz. \tag{13}$$

2.3 Fluid Model

This section presents a brief discussion of the fluid-discretization procedure, while a more thorough discussion can be found in the earlier work of Bhatia and Beran [9, 11]. The governing equations are formulated on the original undeformed configuration and the dynamic influence of structural motion is approximated through the slip-wall boundary conditions.

The Euler equations are written in the conservative form as

$$\frac{\partial \boldsymbol{x}_\mathrm{f}}{\partial t} + \frac{\partial \boldsymbol{f}_i}{\partial x_i} = 0 \; , \tag{14}$$

$$\boldsymbol{f}_i n_i|_\Gamma = \boldsymbol{f}_n \; , \tag{15}$$

where $\boldsymbol{x}_\mathrm{f}$ are the conservative solution variables, and the inviscid advection flux, $\boldsymbol{f}_i = \boldsymbol{f}_i(\boldsymbol{x}_\mathrm{f})$, are defined as

$$\boldsymbol{x}_\mathrm{f} = \left\{ \begin{array}{c} \rho_\mathrm{f} \\ \rho_\mathrm{f}\boldsymbol{v} \\ \rho_\mathrm{f} E_\mathrm{f} \end{array} \right\} \; , \tag{16}$$

and

$$\boldsymbol{f}_i = \left\{ \begin{array}{c} \rho_\mathrm{f} v_i \\ \rho_\mathrm{f}\boldsymbol{v} v_i + p\delta_{ij} \\ v_i(\rho_\mathrm{f} E_\mathrm{f} + p) \end{array} \right\} \; , \tag{17}$$

with $\boldsymbol{v} = \{v_1, v_2, v_3\}$ and $E_\mathrm{f} = c_v T + \boldsymbol{v}^T\boldsymbol{v}/2$. Eq. (15) specifies the boundary-normal flux which is used to define boundary conditions for symmetry, solid-wall and far-field boundaries. Eqs. (14)–(17) along with the equation of state $p = R\rho_\mathrm{f} T$ provide the necessary set of equations to calculate the state of fluid-flow. The speed of sound is calculated as, $a = \sqrt{\gamma RT} = \sqrt{\gamma p/\rho_\mathrm{f}}$, and the surface pressure coefficient is $c_p = (p - p_\infty)/q_\infty$. The advection-flux vectors are also expressed in a linearized form as $\boldsymbol{f}_i = \boldsymbol{A}_i \boldsymbol{x}_\mathrm{f}$, where the matrices $\boldsymbol{A}_i = \partial \boldsymbol{f}_i / \partial \boldsymbol{x}_\mathrm{f}$ are the advection-flux Jacobians.

2.3.1 Steady-State Solution

The variational statement for the steady-state solution is written as [9]: find $\boldsymbol{x}_\mathrm{f}^0 \in \mathcal{V}_\mathrm{f}^h$ such that for all $\boldsymbol{\phi} \in \mathcal{V}_\mathrm{f}^h$

$$\int_\Omega \boldsymbol{\phi}^T \left(\frac{\partial \boldsymbol{x}_\mathrm{f}^0}{\partial t} + \frac{\partial \boldsymbol{f}_i}{\partial x_i} \right) d\Omega + \sum_{e=1}^{N_{el}} \left[\int_{\Omega_e} \frac{\partial \boldsymbol{\phi}^T}{\partial x_i} \boldsymbol{A}_i \boldsymbol{\tau}(\boldsymbol{x}_\mathrm{f}^0) \left(\frac{\partial \boldsymbol{x}_\mathrm{f}^0}{\partial t} + \frac{\partial \boldsymbol{f}_i}{\partial x_i} \right) d\Omega_e + \int_{\Omega_e} \delta(\boldsymbol{x}_\mathrm{f}^0) \frac{\partial \boldsymbol{\phi}^T}{\partial x_i} \frac{\partial \boldsymbol{x}_\mathrm{f}^0}{\partial x_i} d\Omega_e \right] = 0 \,, \quad (18)$$

where, N_{el} is the number of elements. The last term in Eq. (18) is called the discontinuity-capturing term, and it adds isotropic artificial viscosity in regions of high solution gradient, such as shocks. $\boldsymbol{\tau}(\boldsymbol{x}_\mathrm{f}^0)$ and $\delta(\boldsymbol{x}_\mathrm{f}^0)$ are the intrinsic time matrix and dissipation coefficient for the discontinuity capturing operator, respectively [9]. Using integration-by-parts, the variational statement is written as

$$\int_\Omega \boldsymbol{\phi}^T \frac{\partial \boldsymbol{x}_\mathrm{f}^0}{\partial t} d\Omega - \int_\Omega \frac{\partial \boldsymbol{\phi}^T}{\partial x_i} \boldsymbol{f}_i d\Omega + \int_\Gamma \boldsymbol{\phi}^T \boldsymbol{f}_n d\Gamma + \sum_{e=1}^{N_{el}} \left[\int_{\Omega_e} \frac{\partial \boldsymbol{\phi}^T}{\partial x_i} \boldsymbol{A}_i \boldsymbol{\tau}(\boldsymbol{x}_\mathrm{f}^0) \left(\frac{\partial \boldsymbol{x}_\mathrm{f}^0}{\partial t} + \frac{\partial \boldsymbol{f}_i}{\partial x_i} \right) d\Omega_e + \int_{\Omega_e} \delta(\boldsymbol{x}_\mathrm{f}^0) \frac{\partial \boldsymbol{\phi}^T}{\partial x_i} \frac{\partial \boldsymbol{x}_\mathrm{f}^0}{\partial x_i} d\Omega_e \right] = 0 \,, \quad (19)$$

This constitutes a nonlinear system of equations for solution of the steady-state flow condition subject to the rigid panel curvature. The far-field and slip-wall boundary conditions are implemented through the third-term in Eq. (19), where $\boldsymbol{f}_n$ is evaluated for these conditions. The characteristics are used to split the Jacobian for incoming and outgoing fluxes at the far-field boundary [9]. At the slip-wall, the boundary-normal flux is written as

$$\boldsymbol{f}_n|_\mathrm{wall} = \boldsymbol{f}_i \hat{n}_i|_\mathrm{wall} = \boldsymbol{v} \cdot \hat{\boldsymbol{n}} \boldsymbol{f}_\mathrm{wall,1} + \boldsymbol{f}_\mathrm{wall,2}, \quad (20)$$

where, $\boldsymbol{f}_\mathrm{wall,1} = \{\rho_\mathrm{f}, \rho_\mathrm{f} v_1, \rho_\mathrm{f} v_2, \rho_\mathrm{f} v_3, (\rho_\mathrm{f} E_\mathrm{f} + p)\}$, and $\boldsymbol{f}_\mathrm{wall,2} = \{0, pn_1, pn_2, pn_3, 0\}$. The wall-normal velocity, $\boldsymbol{v} \cdot \hat{\boldsymbol{n}}$, is replaced by using the flow tangency condition. If deformation or a rigid shape produces a change in the surface normal, $d\hat{\boldsymbol{n}}$, the tangency condition is written as

$$\boldsymbol{v} \cdot (\hat{\boldsymbol{n}} + d\hat{\boldsymbol{n}}) = \frac{\partial \boldsymbol{u}}{\partial t} \cdot (\hat{\boldsymbol{n}} + d\hat{\boldsymbol{n}}). \quad (21)$$

Then simple algebraic manipulation gives us $\boldsymbol{v} \cdot \hat{\boldsymbol{n}} = \frac{\partial \boldsymbol{u}}{\partial t} \cdot (\hat{\boldsymbol{n}} + d\hat{\boldsymbol{n}}) - \boldsymbol{v} \cdot d\hat{\boldsymbol{n}}$, where $d\hat{\boldsymbol{n}}$ is obtained from a function describing the rigid panel curvature.

2.3.2 Small-Disturbance Solution

Once $\boldsymbol{x}_{\rm f}^0$ is available, it is assumed that the system can experience small disturbances $\boldsymbol{x}_{\rm f}^\Delta$ so that the complete solution is defined as $\boldsymbol{x}_{\rm f} = \boldsymbol{x}_{\rm f}^0 + \boldsymbol{x}_{\rm f}^\Delta$, where

$$\boldsymbol{x}_{\rm f}^\Delta = \left\{ \begin{array}{c} \Delta\rho_{\rm f} \\ \Delta(\rho_{\rm f}\boldsymbol{v}) \\ \Delta(\rho_{\rm f}E_{\rm f}) \end{array} \right\} . \tag{22}$$

The small-disturbance Euler equation is written as

$$\frac{\partial \boldsymbol{x}_{\rm f}^\Delta}{\partial t} + \frac{\partial \boldsymbol{f}_i^\Delta}{\partial x_i} = 0 . \tag{23}$$

Using Eq. (17), the small-disturbance inviscid flux is written as

$$\boldsymbol{f}_i^\Delta = \left\{ \begin{array}{c} v_i\Delta\rho_{\rm f} + \rho_{\rm f}\Delta v_i \\ (\rho_{\rm f}\Delta v_i + v_i\Delta\rho_{\rm f})\boldsymbol{v} + \rho_{\rm f}v_i\Delta\boldsymbol{v} + \Delta p\delta_{ij} \\ (\rho_{\rm f}E_{\rm f} + p)\Delta v_i + (E_{\rm f}\Delta\rho_{\rm f} + \rho_{\rm f}\Delta E_{\rm f} + \Delta p)v_i \end{array} \right\} , \tag{24}$$

where the small-disturbance quantities are defined as, $\Delta v_i = (\Delta(\rho_{\rm f}v_i) - v_i\Delta\rho_{\rm f})/\rho_{\rm f}$, $\Delta E_{\rm f} = (\Delta(\rho_{\rm f}E_{\rm f}) - E_{\rm f}\Delta\rho_{\rm f})/\rho_{\rm f}$, $\Delta k = \boldsymbol{v}\cdot\Delta\boldsymbol{v}$, $\Delta T = (\Delta E_{\rm f} - \Delta k)/c_v$, $\Delta p = R(T\Delta\rho_{\rm f} + \rho_{\rm f}\Delta T)$, $\Delta a = \sqrt{\gamma R/T}\Delta T/2$. The small-disturbance flux is expressed in a linearized form as $\boldsymbol{f}_i^\Delta = \boldsymbol{A}_i\boldsymbol{x}_{\rm f}^\Delta$.

The boundary-normal far-field flux, $\boldsymbol{f}_n^\Delta|_\infty$, is evaluated as

$$\boldsymbol{f}_n^\Delta|_\infty \;\; = \;\; \boldsymbol{A}^{(+)}\boldsymbol{x}_{\rm f}^\Delta + \boldsymbol{A}^{(-)}\boldsymbol{x}_{{\rm f},\infty}^\Delta = \boldsymbol{A}^{(+)}\boldsymbol{x}_{\rm f}^\Delta , \tag{25}$$

where, $\boldsymbol{x}_{{\rm f},\infty}^\Delta = 0$, and the flux Jacobians for outgoing and incoming fluxes, $\boldsymbol{A}^{(+)}$ and $\boldsymbol{A}^{(-)}$, are evaluated from the Riemann invariants at far-field boundary.

The boundary-normal flux, $\boldsymbol{f}_n^\Delta|_{\rm wall}$, on a solid-wall is obtained using Eq. (24) and is expressed as

$$\boldsymbol{f}_n^\Delta|_{\rm wall} = \boldsymbol{f}_i^\Delta n_i|_{\rm wall} = \Delta\boldsymbol{v}\cdot\hat{\boldsymbol{n}}\boldsymbol{f}_{{\rm wall},1}^\Delta + \boldsymbol{f}_{{\rm wall},2}^\Delta , \tag{26}$$

where $\boldsymbol{f}_{{\rm wall},1}^\Delta = \{\rho_{\rm f}, \rho_{\rm f}v_1, \rho_{\rm f}v_2, \rho_{\rm f}v_3, (\rho_{\rm f}E_{\rm f} + p)\}$, and $\boldsymbol{f}_{{\rm wall},2}^\Delta = \{0, \Delta p n_1, \Delta p n_2, \Delta p n_3, 0\}$. An expression for $\Delta\boldsymbol{v}\cdot\hat{\boldsymbol{n}}$ is obtained from the perturbation of Eq. (21):

$$(\boldsymbol{v} + \Delta\boldsymbol{v})\cdot(\hat{\boldsymbol{n}} + d\hat{\boldsymbol{n}} + \Delta\hat{\boldsymbol{n}}) = \frac{\partial(\boldsymbol{u} + \Delta\boldsymbol{u})}{\partial t}\cdot(\hat{\boldsymbol{n}} + d\hat{\boldsymbol{n}} + \Delta\hat{\boldsymbol{n}}), \tag{27}$$

where, $\Delta\hat{\boldsymbol{n}}$ is the perturbation in the surface normal and $\Delta\boldsymbol{u}$ is the perturbation in structural deformation. Then, simple algebraic manipulations leads to $\Delta\boldsymbol{v}\cdot\hat{\boldsymbol{n}} = \frac{\partial(\boldsymbol{u}+\Delta\boldsymbol{u})}{\partial t}\cdot(\hat{\boldsymbol{n}} + d\hat{\boldsymbol{n}} + \Delta\hat{\boldsymbol{n}}) - \boldsymbol{v}\cdot(\hat{\boldsymbol{n}} + d\hat{\boldsymbol{n}} + \Delta\hat{\boldsymbol{n}}) - \Delta\boldsymbol{v}\cdot(d\hat{\boldsymbol{n}} + \Delta\hat{\boldsymbol{n}})$. Finally, neglecting the high-order terms in the perturbation $(\Delta\boldsymbol{v}\cdot\Delta\boldsymbol{n})$ and using Eq. (21) simplifies the expression to

$$\Delta\boldsymbol{v}\cdot\hat{\boldsymbol{n}} = \frac{\partial\boldsymbol{u}}{\partial t}\cdot\Delta\hat{\boldsymbol{n}} + \frac{\partial\Delta\boldsymbol{u}}{\partial t}\cdot(\hat{\boldsymbol{n}} + d\hat{\boldsymbol{n}}) - \boldsymbol{v}\cdot\Delta\hat{\boldsymbol{n}} - \Delta\boldsymbol{v}\cdot d\hat{\boldsymbol{n}} \tag{28}$$

The first two terms on the right-hand-side of Eq. (28) depend on the structural velocity and its perturbation and the last two term depends on the structural deformation and its perturbation through the surface normal.

The variational statement for the small-disturbance solution is written as [9]: find $\boldsymbol{x}_{\mathrm{f}}^{\Delta} \in \mathcal{V}_{\mathrm{f}}^{h}$ such that for all $\boldsymbol{\phi} \in \mathcal{V}_{\mathrm{f}}^{h}$

$$\int_{\Omega} \boldsymbol{\phi}^T \frac{\partial \boldsymbol{x}_{\mathrm{f}}^{\Delta}}{\partial t} d\Omega - \int_{\Omega} \frac{\partial \boldsymbol{\phi}^T}{\partial x_i} \boldsymbol{f}_i^{\Delta} d\Omega + \int_{\Gamma} \boldsymbol{\phi}^T \boldsymbol{f}_n^{\Delta} d\Gamma + \sum_{e=1}^{N_{el}} \left[\int_{\Omega_e} \frac{\partial \boldsymbol{\phi}^T}{\partial x_i} \boldsymbol{A}_i \boldsymbol{\tau}(\boldsymbol{x}_{\mathrm{f}}^0) \left(\frac{\partial \boldsymbol{x}_{\mathrm{f}}^{\Delta}}{\partial t} + \frac{\partial \boldsymbol{f}_i^{\Delta}}{\partial x_i} \right) d\Omega_e + \int_{\Omega_e} \delta(\boldsymbol{x}_{\mathrm{f}}^0) \frac{\partial \boldsymbol{\phi}^T}{\partial x_i} \frac{\partial \boldsymbol{x}_{\mathrm{f}}^{\Delta}}{\partial x_i} d\Omega_e \right] = 0 \ , \quad (29)$$

The values for $\boldsymbol{\tau}(\boldsymbol{x}_{\mathrm{f}}^0)$ and $\delta(\boldsymbol{x}_{\mathrm{f}}^0)$ in Eq. (29) assume their numerical values from the steady-state solution. It should be noted that even in the absence of shocks in the steady-state flow, any discontinuity in the boundary conditions of the small-disturbance problem can propagate into the analysis domain. Such cases can benefit from updating the values of δ using the small-disturbance solution. However, in the present study of small-disturbance solutions, $\delta(\boldsymbol{x}_{\mathrm{f}})$ assumes its value from the steady-state solution, which is zero due to the uniform flow condition for steady-state flow.

Eq. (29) is expressed in matrix-form as

$$\boldsymbol{M}_{\mathrm{ff}} \frac{dX_{\mathrm{f}}^{\Delta}}{dt} + \boldsymbol{J}_{\mathrm{ff}} X_{\mathrm{f}}^{\Delta} + \boldsymbol{J}_{\mathrm{fs}}^0 X_{\mathrm{s}}^{\Delta} + \boldsymbol{J}_{\mathrm{fs}}^1 \frac{dX_{\mathrm{s}}^{\Delta}}{dt} = 0 \ , \quad (30)$$

where $\boldsymbol{J}_{\mathrm{ff}} = \boldsymbol{J}_{\mathrm{ff,flux}} + \boldsymbol{J}_{\mathrm{ff,wall}} + \boldsymbol{J}_{\mathrm{ff},\infty}$ and the individual matrices are related to the variational statement as

$$\Phi^T \boldsymbol{M}_{\mathrm{ff}} \frac{dX_{\mathrm{f}}^{\Delta}}{dt} \equiv \int_{\Omega} \boldsymbol{\phi}^T \frac{\partial \boldsymbol{x}_{\mathrm{f}}^{\Delta}}{\partial t} \, d\Omega + \sum_{e=1}^{N_{el}} \int_{\Omega_e} \frac{\partial \boldsymbol{\phi}}{\partial x_i}^T \boldsymbol{A}_i \boldsymbol{\tau}(\boldsymbol{x}_{\mathrm{f}}^0) \frac{\partial \boldsymbol{x}_{\mathrm{f}}^{\Delta}}{\partial t} \, d\Omega_e \ , \quad (31)$$

$$\Phi^T \boldsymbol{J}_{\mathrm{ff,flux}} X_{\mathrm{f}}^{\Delta} \equiv - \int_{\Omega} \frac{\partial \boldsymbol{\phi}^T}{\partial x_i} \boldsymbol{f}_i^{\Delta} d\Omega + \sum_{e=1}^{N_{el}} \left[\int_{\Omega_e} \frac{\partial \boldsymbol{\phi}}{\partial x_i}^T \boldsymbol{A}_i \boldsymbol{\tau}(\boldsymbol{x}_{\mathrm{f}}^0) \frac{\partial \boldsymbol{f}_i^{\Delta}}{\partial x_i} d\Omega_e + \int_{\Omega_e} \delta(\boldsymbol{x}_{\mathrm{f}}^0) \frac{\partial \boldsymbol{\phi}}{\partial x_i} \frac{\partial \boldsymbol{x}_{\mathrm{f}}^{\Delta}}{\partial x_i} d\Omega_e \right] , \quad (32)$$

$$\Phi^T \boldsymbol{J}_{\mathrm{ff,wall}} X_{\mathrm{f}}^{\Delta} \equiv \int_{\Gamma_{\mathrm{wall}}} \boldsymbol{\phi}^T \boldsymbol{f}_{\mathrm{wall},2}^{\Delta} \, d\Gamma_{\mathrm{wall}} \ , \quad (33)$$

$$\Phi^T \boldsymbol{J}_{\mathrm{ff},\infty} X_{\mathrm{f}}^{\Delta} \equiv \int_{\Gamma_{\infty}} \boldsymbol{\phi}^T \boldsymbol{A}^{(+)} \boldsymbol{x}_{\mathrm{f}}^{\Delta} \, d\Gamma_{\infty} \ , \quad (34)$$

$$\Phi^T \boldsymbol{J}_{\mathrm{fs}}^0 X_{\mathrm{s}}^{\Delta} \equiv - \int_{\Gamma_{\mathrm{wall}}} \boldsymbol{\phi}^T \boldsymbol{v} \cdot \Delta \hat{\boldsymbol{n}} \boldsymbol{f}_{\mathrm{wall},1}^{\Delta} \, d\Gamma_{\mathrm{wall}} \ , \quad (35)$$

$$\Phi^T \boldsymbol{J}_{\mathrm{fs}}^1 \frac{dX_{\mathrm{s}}^{\Delta}}{dt} \equiv \int_{\Gamma_{\mathrm{wall}}} \boldsymbol{\phi}^T \Delta \frac{\partial \boldsymbol{u}}{\partial t} \cdot \hat{\boldsymbol{n}} \boldsymbol{f}_{\mathrm{wall},1}^{\Delta} \, d\Gamma_{\mathrm{wall}} \ . \quad (36)$$

Jacobians for coupling terms in Eqs. (35) and (36) are not explicitly calculated in this implementation. Instead their matrix-vector products are evaluated and used. This is discussed in more detail in the following section.

The procedure for fluid-structure coupling and estimation of stability roots is detailed in the earlier work by Bhatia and Beran [10, 11].

3 Results

This section presents the stability analysis for a semi-infinite panel at Mach 0.9, 1.1 and 1.5 with varying panel curvature defined by $f(x) = \eta \sin(\pi x/L)$. The results include

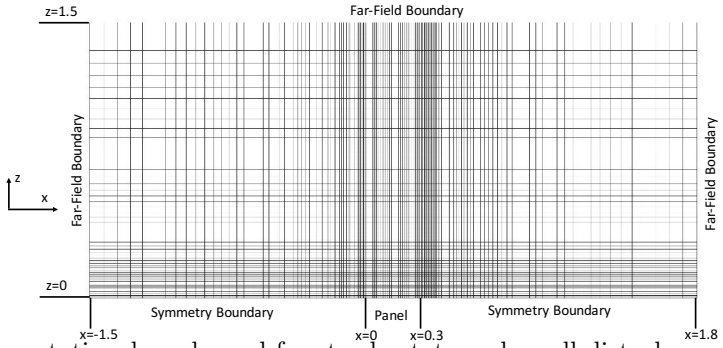

Figure 2: Computational mesh used for steady-state and small-disturbance flow solution.

a plot of flutter speed, V_F, and flutter frequency, ω_F, and modal participation of the primary instability for increasing values of non-dimensional height $\eta = H/L$. For each Mach number the steady flow and instability data are presented for a small value of $\eta = 0.001$, which closely matches the previously published results about a flat panel ($\eta = 0$) [10,11]. The aerodynamic nonlinearity increases with the value of η and causes a change in composition of the flutter mode. In order to quantify the influence of aerodynamic nonlinearity the steady-state Mach number is plotted over the panel surface for several values of η. The Mach number plot helps in identifying the presence of shocks and the sub-/supersonic nature of flow. A second plot of $(M - M_\infty)/\eta \cdot L$ approximates the slope $dM(x,h)/dH$ and provides a clear indication of the departure from linearity, since a linear flow response will lead to a constant value of this slope.

In addition to these plots, the steady-state density contours are presented with a sonic line (when applicable) along with the panel deformation and surface density perturbation for the critical panel instability. These two quantities are scaled by the maximum absolute value of the real part of structural mode, $\max \mathrm{Re}(|u_y|)$. Since the perturbation data is obtained from an eigenvector, any scaling of this quantity is also a solution. Contour plots of the scaled density perturbation in the flow domain are also presented to show the propagation of the perturbations in the flow domain.

Details of the panel length and material are listed in Table 1. The computational domain (Fig. 2) for the fluid flow extends 5 chord-lengths beyond the panel along both the $x-$ and $z-$axes. The domain is discretized using a grid of 150x60 bi-linear elements with 30 elements on the panel and 60 elements between the panel and far-field boundaries in either direction. The elements on the panel are uniformly sized along the $x-$axis, while mesh density is varied from the far-field to the panel such that the element dimension at the far-field boundary is 20 times that at the panel.

All computations are performed with MAST [11, 12]. A direct sparse solver is used to solve the structural system of equations. An iterative GMRES solver with ILU(0) preconditioner is used for the steady-state fluid-equations, while the n complex-valued system of equations are converted into $2n$ real-valued system of equations and solved using an ILU(0) block-preconditioned linear solver [13].

3.1 $M_\infty = 0.9$

Given the proximity of $M_\infty = 0.9$ to the sonic flow condition, the flow is seen to be more sensitive to panel curvature than that observed in the previous section for $M_\infty = 0.7$.

Table 1: Physical parameters for panel and ambient fluid properties

Parameter	Value
Fluid	
Far-field density	1.35 kg/m^3
Far-field temperature	300 K
Specific heat at constant pressure ($c_{p,\mathrm{f}}$)	1003 J/kg/K
Ideal gas constant (R)	287 J/kg/K
Specific heat ratio ($c_{p,\mathrm{f}}/c_{v,\mathrm{f}}$)	1.4
Structural	
Young's modulus (E_s)	72 GPa
Poisson ratio (ν)	0.33
Density (ρ_s)	2700 kg/m^3
Length (L)	0.3 m
Section thickness (h)	0.0015 m
Mass ratio ($\mu = \rho_\mathrm{f} L/\rho_\mathrm{s} h$)	0.1
Section rigidity ($D = E_\mathrm{s} h^3/12(1-\nu^2)$)	22.7

The surface Mach number for various values of η (see Fig. 3(a)) shows the formation of a small supersonic region over the panel for $\eta = 0.01$ with a shock at approximately 65% chord location. Increasing η results in a stronger shock located further downstream and for the case of $\eta = 0.05$, the shock is at the trailing edge of the panel. The change in surface Mach number with respect to H in Fig. 3(b) shows that the flow departs from linear condition at $\eta = 0.01$.

The influence of aerodynamic nonlinearity on the flutter characteristics is evident from the plots in Fig. 4. Increasing η initially results only in a reduction of flutter speed while keeping the instability as a single degree-of-freedom zero frequency divergence mode. The appearance of a shock at $\eta = 0.01$ results in a monotonic increase of the instability speed and changes the divergence mode composition to the first two panel bending modes. At $\eta = 0.02$, the instability mode changes from divergence to flutter. While the flutter mode is a combination of the first two panel bending modes with a dominant first mode, the importance of the second bending mode continues to increase monotonically.

The contour plots for steady-state density and its perturbation in the divergence mode at $\eta = 0.001$ (Fig. 5) show that a panel deformation into the flow causes the flow to accelerate with a reduction in density, and vice-a-versa for deformation away from the flow.

The supersonic region over the curved panel at $\eta = 0.02$ is identified by the sonic line in Fig. 6(a). The instability in this case is a zero frequency divergence mode. The panel deformation and the corresponding density perturbation are shown in Fig. 6(c). Since the maximum value of the perturbation is dictated by the resolution at the shock location, the $y-$axis limits of this plot are chosen to focus on the density perturbation on the entire panel. The mixed flow significantly alters the nature of perturbations on the panel in comparison with the previous case at $\eta = 0.001$.

At $\eta = 0.03$ the size of the supersonic bubble increases (Fig.7(a)) and changes the instability from divergence to flutter. The panel deformation and corresponding surface

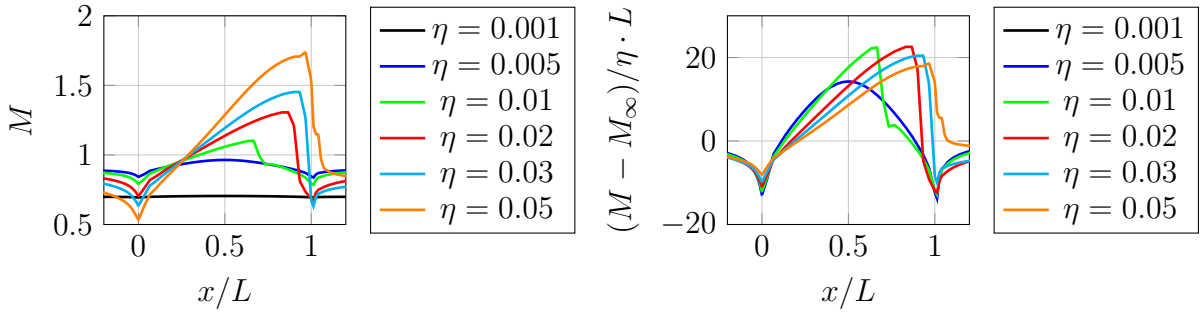

(a) Mach number (b) Change in Mach number

Figure 3: Surface Mach number and change with respect to H for increasing value of η at $M_\infty = 0.9$

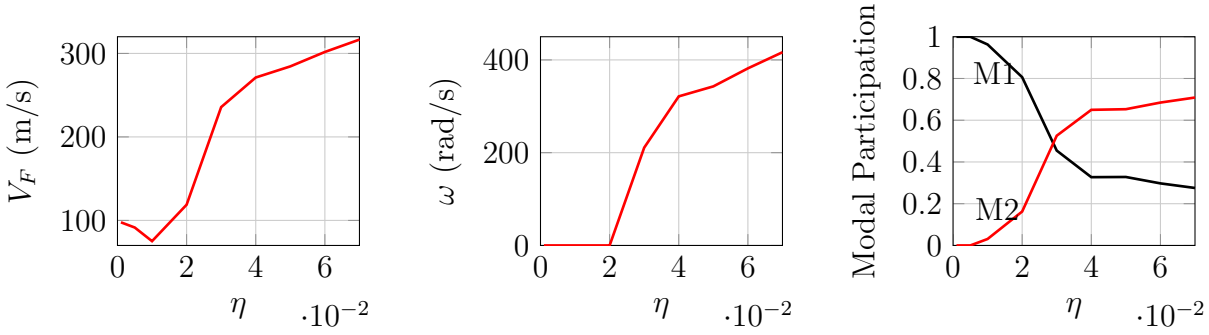

(a) Flutter Speed (b) Flutter frequency (c) Modal participation

Figure 4: Influence of η on flutter speed, flutter frequency and modal participation at $M_\infty = 0.9$.

density perturbations are shown in Figs. 7(b) and 7(c), respectively. The contour plots of density perturbation in Fig. 8 show an interesting trend. While the perturbations in the supersonic bubble are able to propagate along the directions of the characteristics, which are dictated by the local Mach number, outside of that the perturbation waves propagate in all directions shown by the alternating red and blue contours.

3.2 $M_\infty = 1.1$

Any curvature at supersonic Mach numbers creates a compression shock for positive surface slope (along the flow direction) and an expansion of the flow for negative slope. The

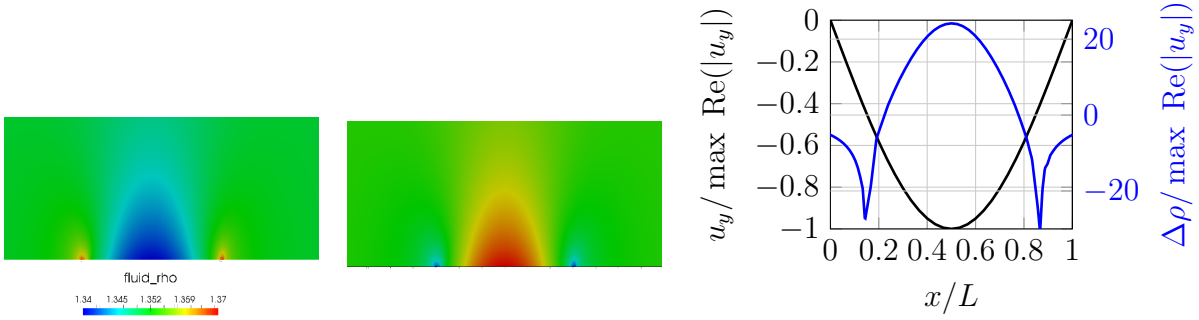

(a) Steady-state density contour

(b) Divergence density perturbation. Red (blue) implies positive (negative) perturbation.

(c) Divergence Mode

Figure 5: Steady-state solution and divergence mode for $M_\infty = 0.9$ at $\eta = 0.001$.

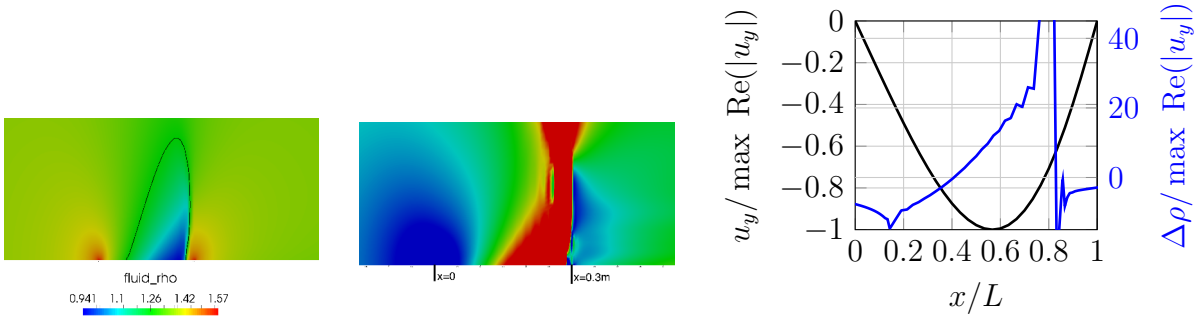

(a) Steady-state density contour

(b) Divergence density perturbation. Red (blue) implies positive (negative) perturbation.

(c) Divergence Mode

Figure 6: Steady-state solution and divergence mode for $M_\infty = 0.9$ at $\eta = 0.02$.

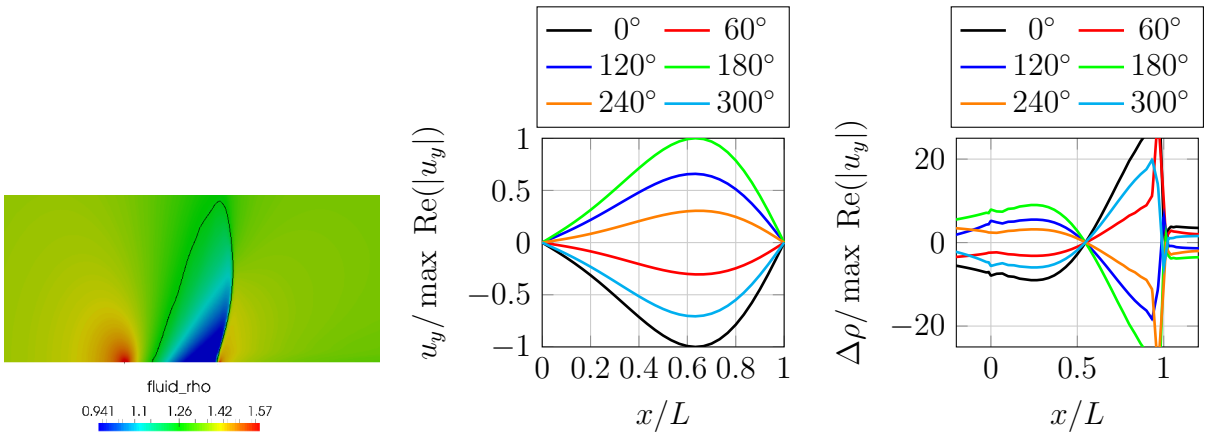

(a) Steady-state density contour

(b) Flutter Mode

(c) Surface density perturbation

Figure 7: Steady-state solution and flutter mode for $M_\infty = 0.9$ at $\eta = 0.03$. The normalized panel deformation and surface density perturbation are plotted for one cycle of the flutter mode.

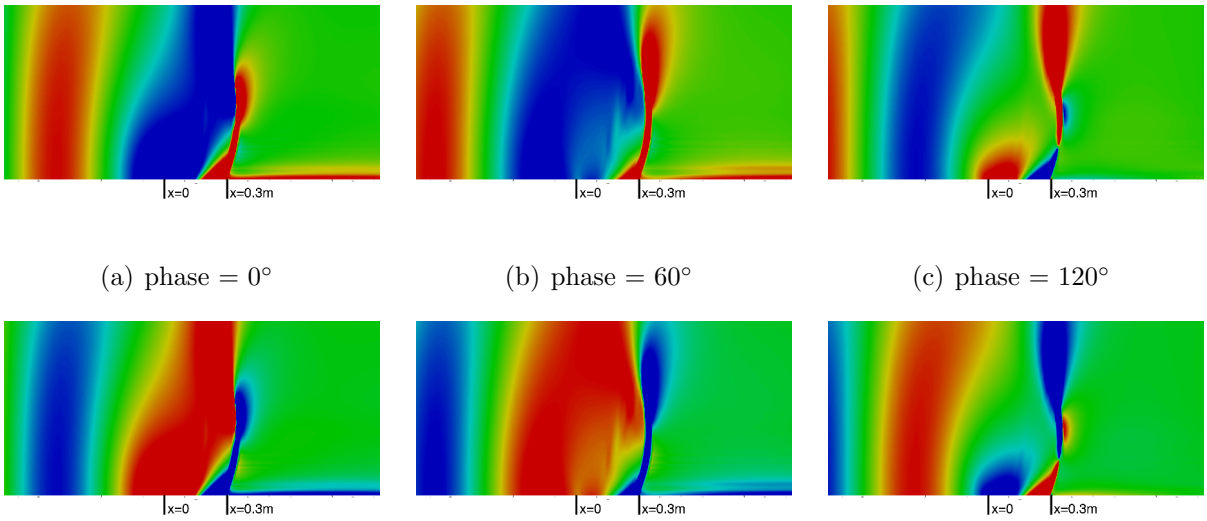

(a) phase = 0°

(b) phase = 60°

(c) phase = 120°

(d) phase = 180°

(e) phase = 240°

(f) phase = 300°

Figure 8: Contour plots of density perturbation at multiple instances in the flutter mode for $M_\infty = 0.9$ at $\eta = 0.03$. Red (blue) implies positive (negative) perturbation.

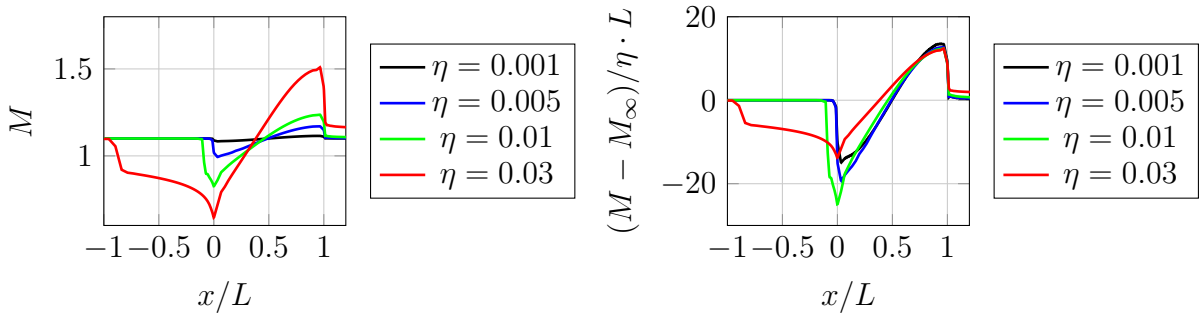

(a) Mach number (b) Change in Mach number

Figure 9: Surface Mach number and change with respect to H for increasing value of η at $M_\infty = 1.1$

reduction in Mach number due to the compression shock for high values of η can create pockets of subsonic region. This is clearly seen in Fig. 9(a) where the shock at the leading edge for $\eta = 0.005$ reduces the Mach number to 1. For higher values of η a normal shock ahead of the panel creates a region of subsonic flow. The slope of change in Mach number with respect to H (Fig. 9(b)) shows the influence of nonlinearity around the leading edge at $\eta = 0.005$, with a larger region of nonlinear influence around the leading edge.

The influence of this nonlinearity is visible in Fig. 10. While the flutter speed increases monotonically with η, the flutter frequency reduces till $\eta = 0.01$ and then increases as the second panel bending mode starts to dominate the panel dynamics.

The steady-state density contour at $\eta = 0.001$ shows the compression and expansion shocks in Fig. 11(a). The panel flutter mode is plotted at multiple instances during the period of the instability in Fig. 11(b). The corresponding surface density perturbations (Fig. 11(c)) and their contour plots (Fig. 12) show that the perturbations are convecting along the characteristic directions in the flow.

The steady-state density contour at $\eta = 0.01$ shows a subsonic region around the panel leading edge (Fig. 13(a)). The flutter mode is dominated by the first panel bending mode (Fig. 13(b)) and the corresponding surface density perturbations show significant amplitudes at the shock location (Fig.13(c)). The density perturbation contour plots in Fig. 14 show that the perturbations around the leading edge propagate upstream till they reach the normal shock, at which point they propagate along the shock.

A similar, but more intensified response can be seen for $\eta = 0.03$ where the normal shock has moved further upstream (Fig. 15(a)) with a larger subsonic region. While the Mach number reduces around the leading edge, the flow is seen to accelerate after 50% chord location. This acceleration of the flow considerably changes the direction of the local characteristics and makes a stronger shock at the trailing edge. The panel flutter mode has a significant contribution from the second panel bending mode (Fig. 15(b)). The density perturbations (Fig. 16) in the subsonic region propagate upstream towards the normal shock, after which they convect along the shock. The modified characteristics around the trailing edge result in stronger perturbations that propagate along the trailing edge shock.

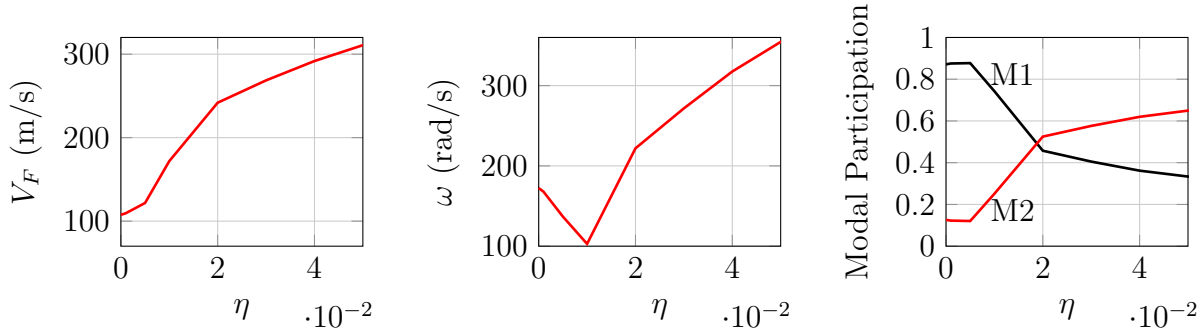

(a) Flutter Speed (b) Flutter frequency (c) Modal participation

Figure 10: Influence of η on flutter speed, flutter frequency and modal participation at $M_\infty = 1.1$.

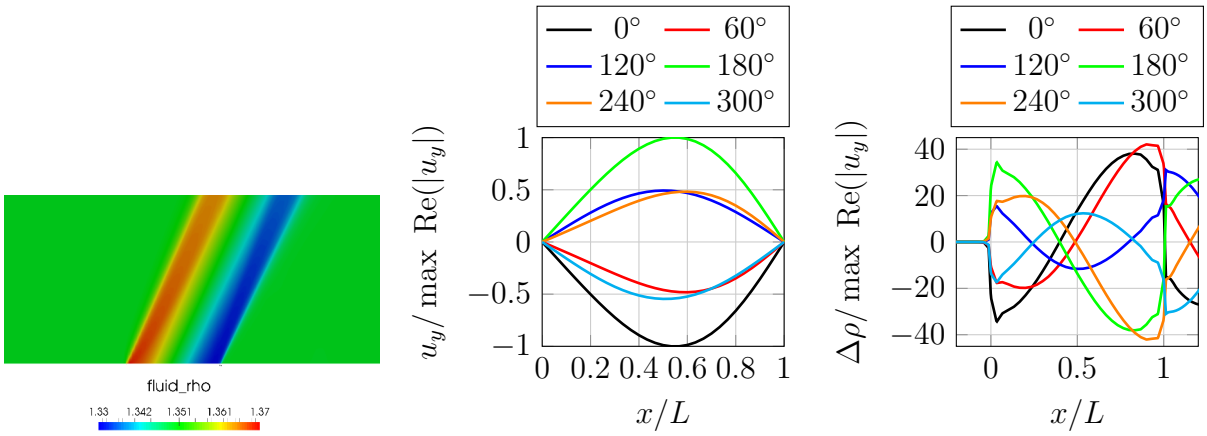

(a) Steady-state density contour (b) Flutter Mode (c) Surface density perturbation

Figure 11: Steady-state solution and flutter mode for $M_\infty = 1.1$ at $\eta = 0.001$. The normalized panel deformation and surface density perturbation are plotted for one cycle of the flutter mode.

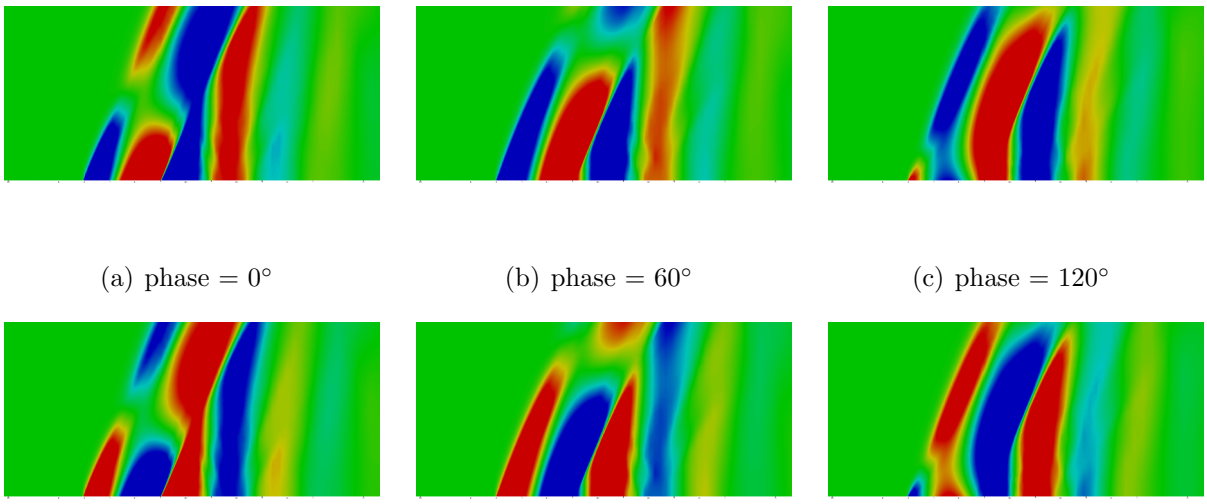

(a) phase = 0° (b) phase = 60° (c) phase = 120°

(d) phase = 180° (e) phase = 240° (f) phase = 300°

Figure 12: Contour plots of density perturbation at multiple instances in the flutter mode for $M_\infty = 1.1$ at $\eta = 0.001$. Red (blue) implies positive (negative) perturbation.

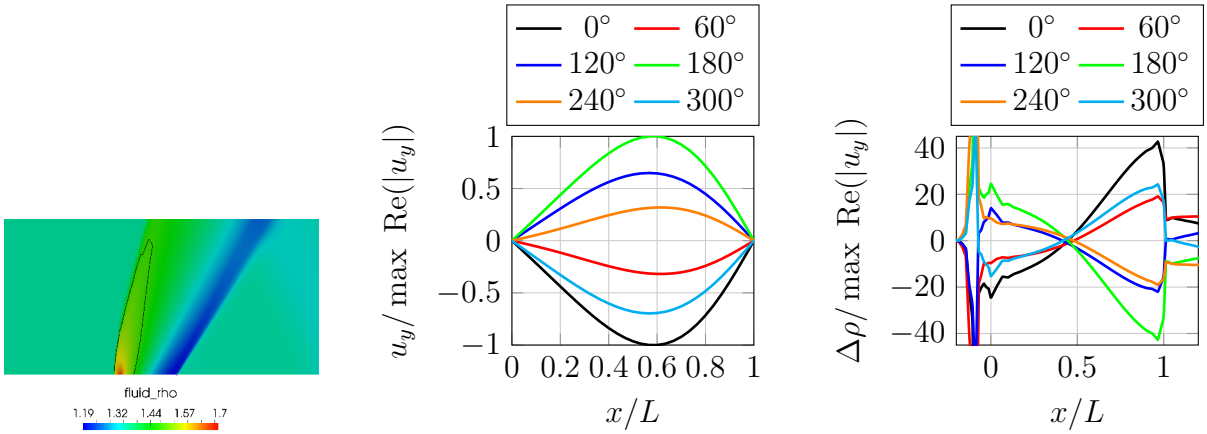

(a) Steady-state density contour. Solid line indicates sonic line.

(b) Flutter Mode

(c) Surface density perturbation

Figure 13: Steady-state solution and flutter mode for $M_\infty = 1.1$ at $\eta = 0.01$. The normalized panel deformation and surface density perturbation are plotted for one cycle of the flutter mode.

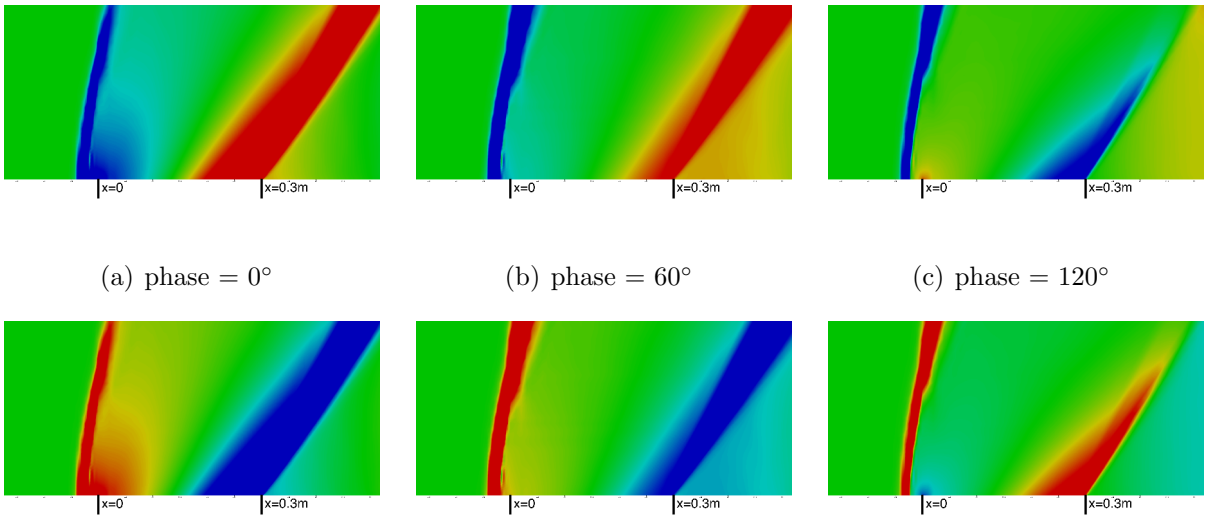

(a) phase = 0°

(b) phase = 60°

(c) phase = 120°

(d) phase = 180°

(e) phase = 240°

(f) phase = 300°

Figure 14: Contour plots of density perturbation at multiple instances in the flutter mode for $M_\infty = 1.1$ at $\eta = 0.01$. Red (blue) implies positive (negative) perturbation.

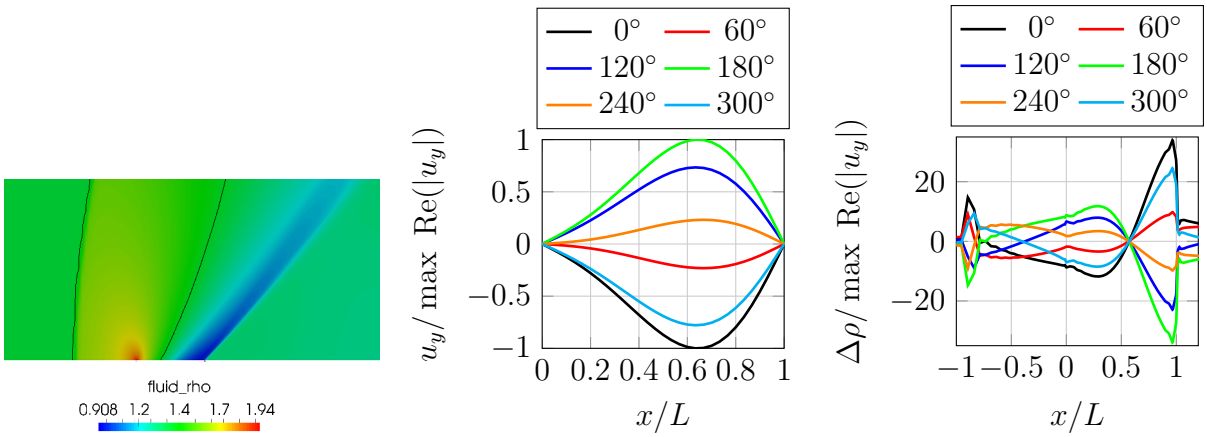

(a) Steady-state density contour (b) Flutter Mode (c) Surface density perturbation

Figure 15: Steady-state solution and flutter mode for $M_\infty = 1.1$ at $\eta = 0.03$. The normalized panel deformation and surface density perturbation are plotted for one cycle of the flutter mode.

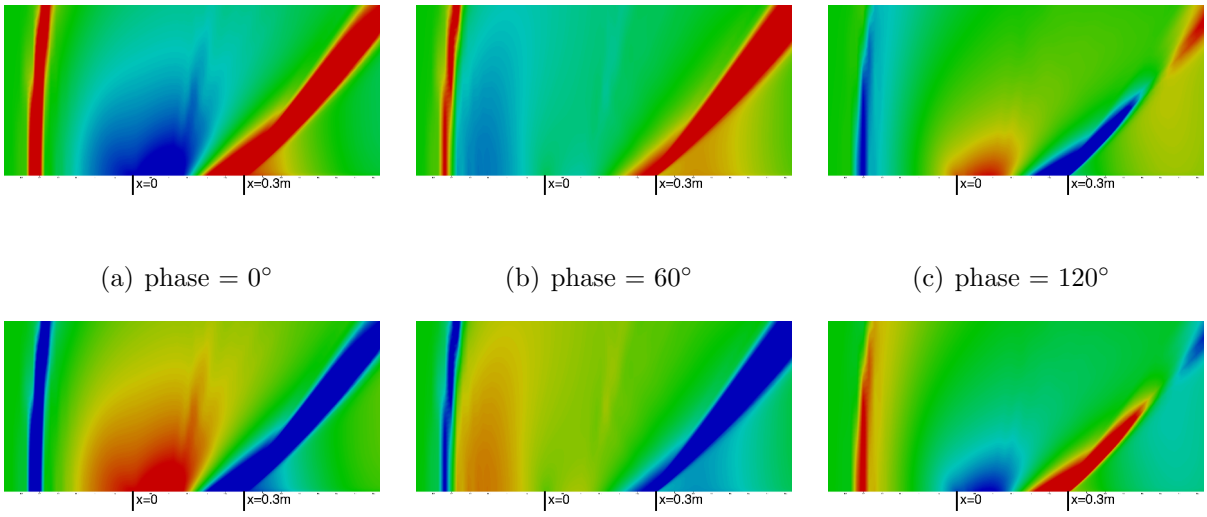

(a) phase = 0° (b) phase = 60° (c) phase = 120°

(d) phase = 180° (e) phase = 240° (f) phase = 300°

Figure 16: Contour plots of density perturbation at multiple instances in the flutter mode for $M_\infty = 1.1$ at $\eta = 0.03$. Red (blue) implies positive (negative) perturbation.

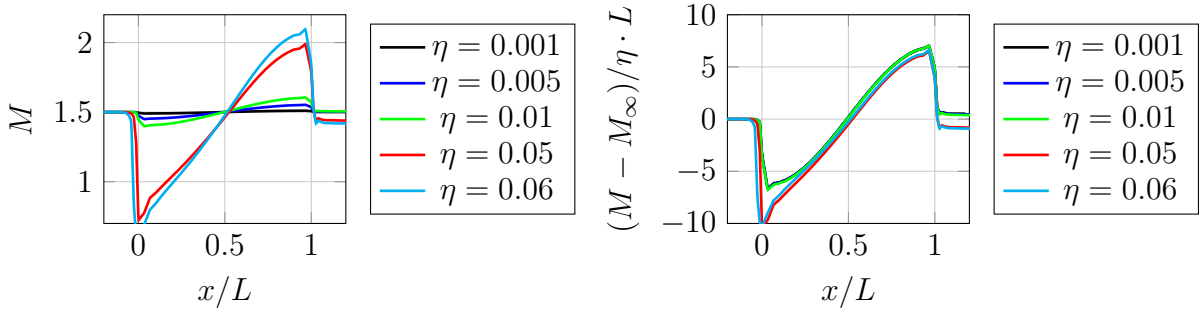

(a) Mach number (b) Change in Mach number

Figure 17: Surface Mach number and change with respect to H for increasing value of η at $M_\infty = 1.5$

3.3 $M_\infty = 1.5$

Steady supersonic flow at $M_\infty = 1.5$ over the curved panel experiences compression from the leading-edge to semi-chord and expansion from semi-chord to the trailing edge (Fig. 17(a)). The compression shock creates a subsonic region around the leading edge for $\eta = 0.05$ and this leads to departure from linear behavior, as seen in Fig. 17(b).

The flutter characteristics at $M_\infty = 1.5$ are found to be extremely sensitive to curvature in the panel. Increasing η to 0.03 causes a drop in the flutter speed to 25% of its value for a flat panel (Fig. 18(a)). The critical mode for a flat panel is the high-frequency third panel bending mode. This quickly changes to a mode composed of the first two panel bending modes (Fig. 18(c)) at a considerably lower frequency.

The steady-state density contour at $\eta = 0.001$ show the compression and expansion shocks along the characteristic lines (Fig. 19(a)). For such a small curvature the flutter mode retains the same characteristic as that for the flat panel, which is a single degree-of-freedom mode primarily composed of the second and third panel bending modes, with a dominant third mode. The surface density perturbation in the flutter mode (Fig. 19(c)) is seen to be proportional to the panel deformation (Fig. 19(b)), which is a trait of supersonic flows. The density perturbation contour plots in Fig. 20 show that the perturbations are propagating along the characteristic directions.

The panel curvature at $\eta = 0.01$ creates a compression and expansion shock structure (Fig. 21(a)) that changes the flutter instability to a composition of the first and second panel bending modes. It is noted that the two bending modes are in-phase, which makes the flutter mode appear as a single degree-of-freedom mode (Fig. 21(b)). The corresponding surface density perturbation are proportional to the local panel slope (Fig. 19(c)). The contours show propagation of the density perturbation along the characteristics in Fig. 22.

3.4 Discussion

The results presented here show that flutter of curved panels at transonic Mach numbers is significantly influenced by aerodynamic nonlinearity. It is important to put these results into a perspective that clearly states the involved assumptions and their implications.

Calculation of the steady-state flow assumes a rigid aerodynamic shape defined by a half-sine bump, and the influence of aerodynamic flow on steady-state panel deformation is neglected. This is a uni-directional coupling for the steady-state flow. This simplification

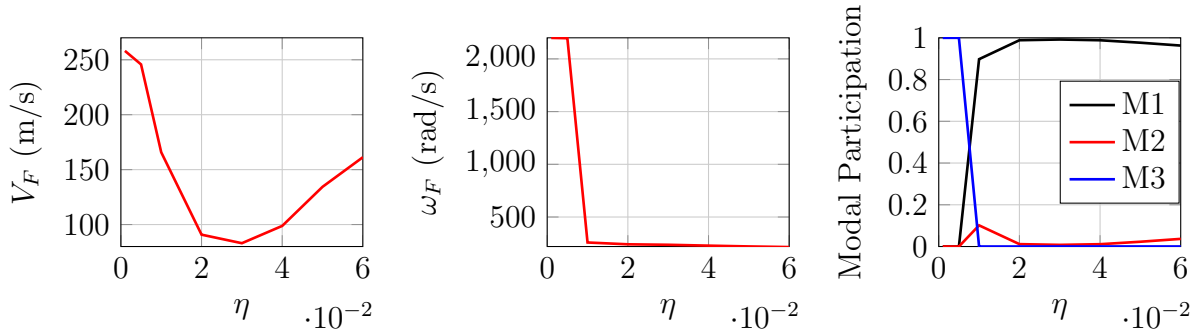

(a) Flutter speed (b) Flutter frequency (c) Modal participation

Figure 18: Influence of η on flutter speed, flutter frequency and modal participation at $M_\infty = 1.5$.

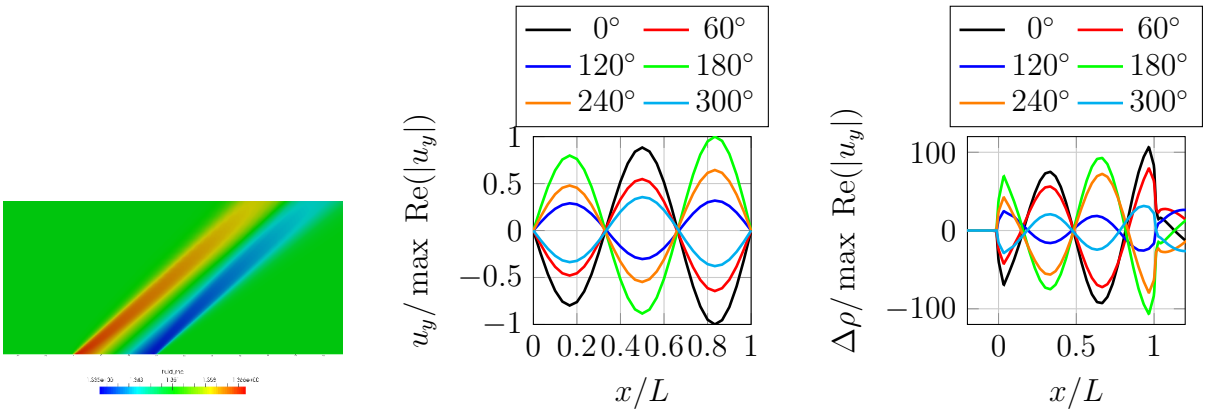

(a) Steady-state density contour (b) Flutter Mode (c) Surface density perturbation

Figure 19: Steady-state solution and flutter mode for $M_\infty = 1.5$ at $\eta = 0.001$. The normalized panel deformation and surface density perturbation are plotted for one cycle of the flutter mode.

was introduced due to the stated purpose of solely focussing on the influence of aerodynamic nonlinearity on flutter speed. It is expected that steady-state panel deformation due to a bi-directional coupling will reduce the curvature observed by the aerodynamic flow. This will likely reduce the severity of the results seen here, although the influence will depend on the dynamic pressure at which instability occurs. Furthermore, an appropriate modeling of this coupling would require that structural nonlinearity due to in-plane stresses be considered. Snap-through behavior has been reported for cases at high dynamic pressure, which is typically associated with higher Mach numbers that those studied here.

The instability analysis assumes small-disturbances about the steady-state condition, which helps in identifying the Hopf bifurcation point. Bhatia and Beran [10, 11] have demonstrated that such an analysis provides credible results that compare favorably with previously reported instability studies using nonlinear time-accurate methodology. However, it can also be argued that when the amplitude of oscillation of a flat panel ($\eta = 0$) is allowed to increase in a nonlinear dynamic analysis, the resulting aerodynamic nonlinearity can influence the stability characteristics in a manner shown here. Such a response, however, will involve shocks that appear and disappear during each cycle of oscillation. The discussion of such dynamics will require a nonlinear time-periodic context involving concepts such as sub-critical or super-critical bifurcation. Accurate analysis of such responses will also require the inclusion of structural nonlinearity as large transverse de-

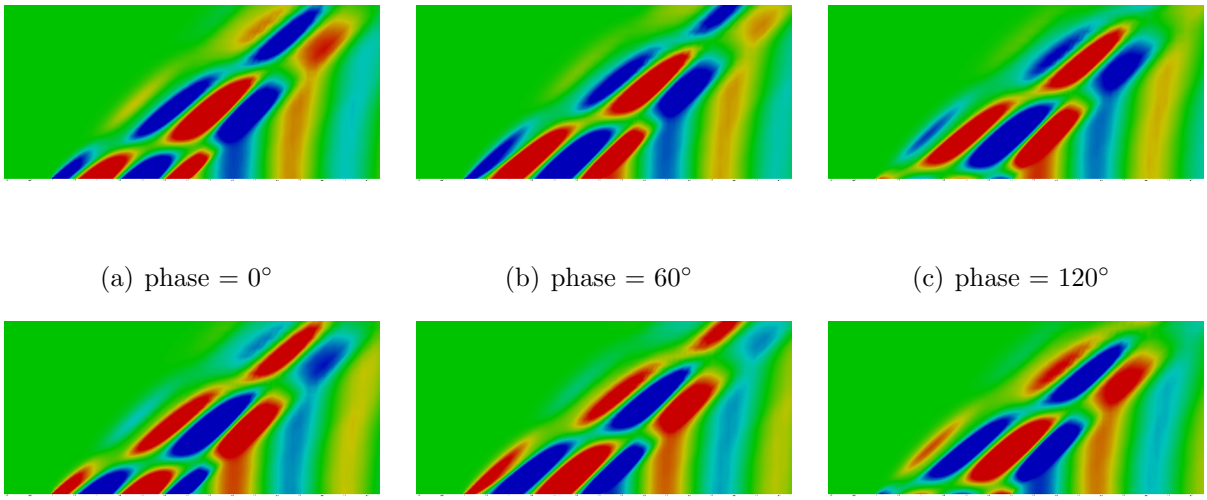

(a) phase = 0° (b) phase = 60° (c) phase = 120°

(d) phase = 180° (e) phase = 240° (f) phase = 300°

Figure 20: Contour plots of density perturbation at multiple instances in the flutter mode for $M_\infty = 1.5$ at $\eta = 0.001$. Red (blue) implies positive (negative) perturbation.

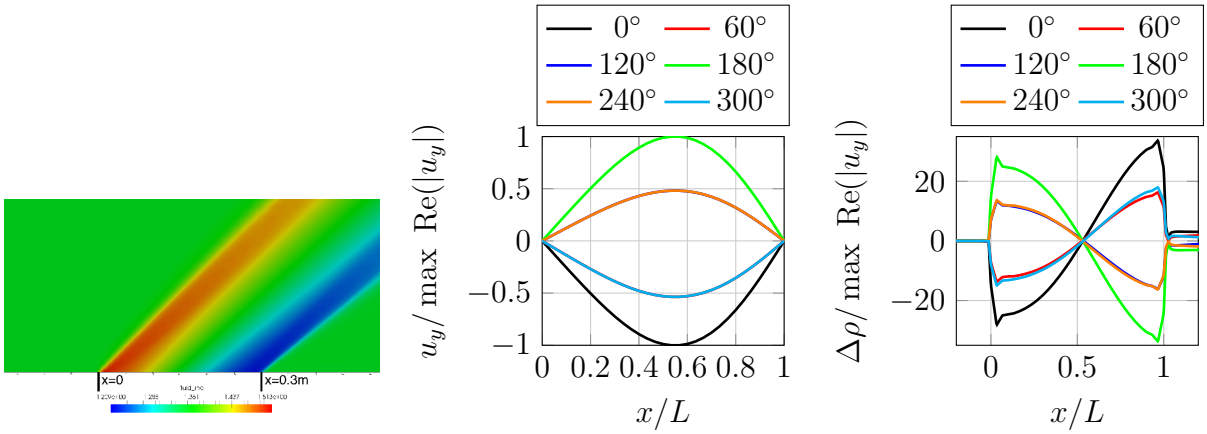

(a) Steady-state density contour (b) Flutter Mode (c) Surface density perturbation

Figure 21: Steady-state solution and flutter mode for $M_\infty = 1.5$ at $\eta = 0.01$. The normalized panel deformation and surface density perturbation are plotted for one cycle of the flutter mode.

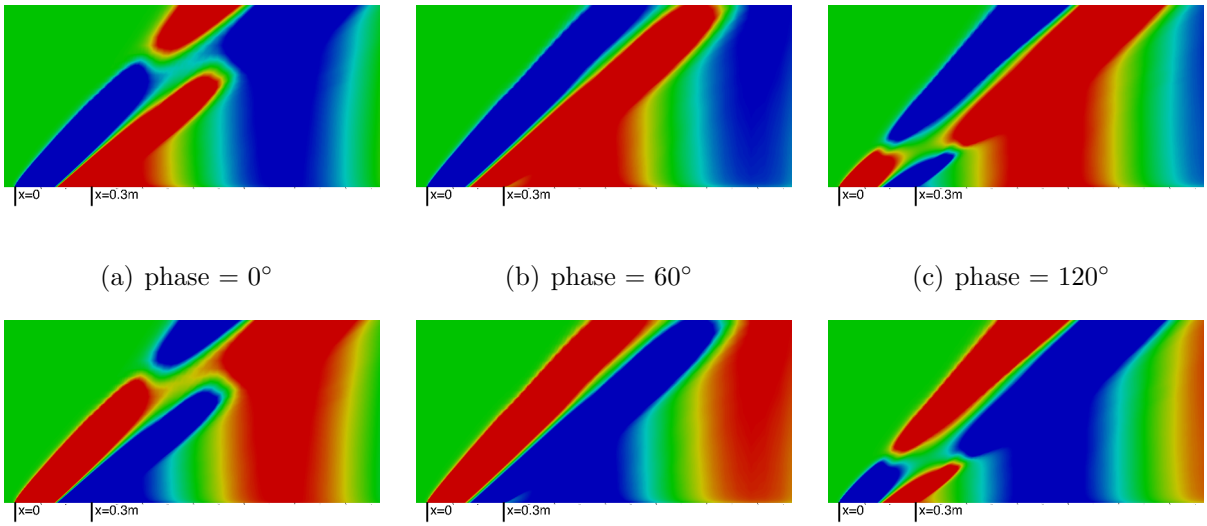

(a) phase = 0° (b) phase = 60° (c) phase = 120°

(d) phase = 180° (e) phase = 240° (f) phase = 300°

Figure 22: Contour plots of density perturbation at multiple instances in the flutter mode for $M_\infty = 1.5$ at $\eta = 0.01$. Red (blue) implies positive (negative) perturbation.

formation will cause the generation of large in-plane stresses.

Finally, the context of this paper only includes inviscid flow. The interaction of boundary layers and shocks in transonic flow can lead to flow separation and shock oscillation, which is outside the scope of this paper.

4 Conclusions

The results shown here demonstrate that aerodynamic nonlinearity in inviscid transonic flow over a curved panel can change the nature of instability from divergence to flutter, and also increase or decrease the speed at which instability occurs. For subsonic flow the instability speed reduces before increasing with the appearance of a supersonic bubble over the panel. At $M_\infty = 1.1$ while the flutter speed increases monotonically with the occurrence of a subsonic region behind a normal shock, the flutter mode changes composition from a multiple degrees-of-freedom to a single degree-of-freedom flutter mode. At $M_\infty = 1.5$ the flutter speed reduces by 68% before increasing again and at $M_\infty = 2.0$ the flutter speed shows an 80% drop from the value for a flat panel.

Future work will include the bi-directional coupling to calculate the steady-state condition and its influence on dynamic instability in a small- and large-disturbance context.

5 References

[1] Bendiksen, O. O. (2011). Review of unsteady transonic aerodynamics theory and applications. *Progress in Aerospace Sciences*, 47(2), 135–167.

[2] (2016). *Design of Thermally-Stressed Panels Subject to Transonic Flutter Constraints*.

[3] Bhatia, M. and Beran, P. S. Design of thermally-stressed panels subject to transonic flutter constraints. *Journal of Aircraft, to appear*.

[4] DOWELL, E. H. (1969). Nonlinear flutter of curved plates. *AIAA Journal*, 7(3), 424–431.

[5] DOWELL, E. H. (1970). Nonlinear flutter of curved plates. ii. *AIAA Journal*, 8(2), 259–261.

[6] Cheng, G. and Mei, C. (2004). Finite element modal formulation for hypersonic panel flutter analysis with thermal effects. *AIAA journal*, 42(4), 687–695.

[7] Abbas, L. K., Rui, X., Marzocca, P., et al. (2011). A parametric study on supersonic/hypersonic flutter behavior of aero-thermo-elastic geometrically imperfect curved skin panel. *Acta mechanica*, 222(1), 41–57.

[8] Culler, A. J. and McNamara, J. J. (2011). Impact of fluid-thermal-structural coupling on response prediction of hypersonic skin panels. *AIAA Journal*, 49(11), 2393–2406.

[9] Bhatia, M. and Beran, P. (2015). h-adaptive stabilized finite-element solver for calculation of generalized aerodynamic forces. *AIAA Journal*, 53(3), 554–572.

[10] Bhatia, M. and Beran, P. S. (2014). Higher-order transonic flutter solutions. In *AIAA 2014-0336, 55th AIAA/ASME/ASCE/AHS/SC Structures, Structural Dynamics, and Materials Conference*. Reston, Virginia.

[11] Bhatia, M. and Beran, P. Panel flutter predictions at transonic and low-supersonic mach numbers using a linearized stability formulation. *AIAA Journal, to appear*.

[12] Bhatia, M. (2016). MAST Web page. `https://github.com/MASTmultiphysics/mast-multiphysics`.

[13] Day, D. and Heroux, M. A. (2001). Solving complex-valued linear systems via equivalent real formulations. *SIAM Journal on Scientific Computing*, 23(2), 480–498.

Copyright statement

Acknowledgements

The material was assigned a clearance on 24 May 2017 under the case number 88ABW-2017-2543. The first author is grateful for the support from Ohio Aerospace Institute under the sub-contract OAI-MSU-1700004. The work of the second author is sponsored by the Air Force Office of Scientific Research under Laboratory Task 12RB06COR (monitored by Dr. Jean-Luc Cambier).